



**HAL**  
open science

## **In-situ kinetics of modifications induced by swift heavy ions in Al<sub>2</sub>O<sub>3</sub>: Colour centre formation, structural modification and amorphization**

C. Grygiel, F. Moisy, M. Sall, Henning Lebius, E. Balanzat, T. Madi, T. Been, D. Marie, I. Monnet

### ► To cite this version:

C. Grygiel, F. Moisy, M. Sall, Henning Lebius, E. Balanzat, et al.. In-situ kinetics of modifications induced by swift heavy ions in Al<sub>2</sub>O<sub>3</sub>: Colour centre formation, structural modification and amorphization. *Acta Materialia*, 2017, 140, pp.157-167. 10.1016/j.actamat.2017.08.028 . hal-03150756

**HAL Id: hal-03150756**

**<https://hal.science/hal-03150756>**

Submitted on 8 Mar 2021

**HAL** is a multi-disciplinary open access archive for the deposit and dissemination of scientific research documents, whether they are published or not. The documents may come from teaching and research institutions in France or abroad, or from public or private research centers.

L'archive ouverte pluridisciplinaire **HAL**, est destinée au dépôt et à la diffusion de documents scientifiques de niveau recherche, publiés ou non, émanant des établissements d'enseignement et de recherche français ou étrangers, des laboratoires publics ou privés.

**In-situ kinetics of modifications induced by swift heavy ions in Al<sub>2</sub>O<sub>3</sub>: colour centre formation, structural modification and amorphization.**

C. Grygiel\*, F. Moisy, M. Sall, H. Lebius, E. Balanzat, T. Madi, T. Been, D. Marie, and I. Monnet,

*CIMAP, CEA – CNRS – ENSICAEN – UNICAEN – Normandie Université, BP 5133, 14070 Caen Cedex 5, FRANCE*

**ABSTRACT**

This paper details in-situ studies of modifications induced by swift heavy ion irradiation in  $\alpha$ -Al<sub>2</sub>O<sub>3</sub>. This complex behaviour is intermediary between the behaviour of amorphizable and non-amorphizable materials, respectively. A unique combination of irradiation experiments was performed at the IRRSUD beam line of the GANIL facility, with three different characterisation techniques: in-situ UV-Vis absorption, in-situ grazing incidence X-Ray diffraction and ex-situ transmission electron microscopy. This allows a complete study of point defects, and by depth profile of structural and microstructural modifications created on the trajectory of the incident ion. The  $\alpha$ -Al<sub>2</sub>O<sub>3</sub> crystals have been irradiated by 92 MeV Xenon and 74 MeV Krypton ions, the irradiation conditions have been chosen rather similar with an energy range where the ratio between electronic and nuclear stopping power changes dramatically as function of depth penetration. The main contribution of electronic excitation, above the threshold for track formation, is present beneath the surface to finally get almost only elastic collisions at the end of the projected range. Amorphization kinetics by the overlapping of multiple ion tracks is observed. In the crystalline matrix, long range strains, unit-cell swelling, local microstrain, domain size decrease, disordering of oxygen sublattice as well as colour centre formation are found. This study highlights the relationship between ion energy losses into a material and its response. While amorphization requires electronic stopping values above a certain threshold, point defects are predominantly induced by elastic collisions, while some structural modifications of the crystalline matrix, such as unit-cell swelling, are due to a contribution of both electronic and nuclear processes.

*Keywords:* Phase transformations; Phase stability; Ion irradiation; X-ray diffraction

---

\* Corresponding author : Tel.: +33 2 31 45 49 34; E-mail adress: grygiel@ganil.fr (C. Grygiel)

## 1. Introduction

The aluminium oxide  $\text{Al}_2\text{O}_3$  crystallized in the alpha phase is a versatile material with a high band gap (9 eV), good dielectric properties, high chemical stability, high refractory behaviour ( $T_m=2318$  K), good transparency in the UV-Visible-IR wavelength range (0.2-6  $\mu\text{m}$ ), and many other properties making this material a good choice for a broad range of applications [1]. Among the potential uses of  $\text{Al}_2\text{O}_3$ , the material can be exposed to extreme conditions like temperature, pressure or radiation under working conditions. Since many years, studies on  $\text{Al}_2\text{O}_3$  under various radiation conditions, like electrons, gammas and especially ions, have been performed in order to understand the role of defects on the stability and the evolution of its physical properties [2-4]. For low energy ion irradiation, the projectile energy is deposited in the target by elastic collisions where the nuclear stopping power ( $S_n$ ) is dominant [5-7]. In this energy range,  $\alpha\text{-Al}_2\text{O}_3$  is known to exhibit colour centre formation, material swelling showing saturation at high fluence, and dislocation loop formation at high temperatures [8]. Moreover, very high fluences or displacements per atom (dpa) have to be reached to observe strong atomic disordering and structure amorphization, even at low temperatures, revealing a relatively good radiation resistance in this energy range [3,9-12]. However, in the case of high energy ion irradiation, the projectile energy is deposited in the target through an inelastic process inducing electronic excitations, the electronic stopping power ( $S_e$ ) being the dominant parameter [13-15].  $\text{Al}_2\text{O}_3$  exhibits material disordering and an easy amorphization at the surface since  $S_e$  is above the threshold value  $S_{\text{eth}}$  [2,16-25]. Moreover, additional structural effects are independently reported in the literature, such as different sensitivities to disorder of O or Al sublattices

[26], swelling [27], lattice deformation [28-30], or a complex track structure along the ion path [25,31].

In the literature dealing with  $\text{Al}_2\text{O}_3$  under high energy ion irradiation, the focus is on the determination of the  $S_{\text{eth}}$ . But there is no straightforward definition of such a threshold. Indeed, full amorphization in the wake of a single ion is only observed with swift heavy clusters [17] that have higher  $S_e$  than monoatomic ions [16,25]. With monoatomic ions, in the single impact regime, *i. e.* at low fluence without significant ion track overlapping, tracks are not fully amorphous. In this regime, a  $S_{\text{eth}}$  for track generation necessarily refers to a threshold for a specific observed damage, and consequently may vary depending on the observations made, *i. e.* the TEM observations of changes along the ion track may provide a different threshold than the one by AFM observation of surface nanodots [20,25,27]. Full amorphization can be triggered with monoatomic ions only at high fluences, due to track overlapping, starting at the surface [18,22]. No amorphous layer has been observed at the implantation depth, where nuclear stopping is predominant. The  $S_{\text{eth}}$  associated to this effect differs in essence from the thresholds of the low fluence regime. Velocity effects [32] and complementary effects of additivity or synergy between the different processes of projectile energy loss might also be considered in the threshold determination for track formation as  $S_{\text{eth}}$  might be appreciably affected by them [27,33-35]. The  $S_{\text{eth}}$  determination for  $\text{Al}_2\text{O}_3$  is difficult, at least partially because its behaviour to SHI irradiation is intermediary between direct amorphizable and non-amorphizable materials. In recent papers dealing with aluminium oxide, these difficulties or artefacts for  $S_{\text{eth}}$  determination are well reported and complete data compiling is detailed, predicting a  $S_{\text{eth}}$  for a high fluence amorphization in

Al<sub>2</sub>O<sub>3</sub> in the range of 9.5-10.5 keV/nm [21,25,27]. By now, this value around 10 keV/nm makes consensus in the community.

Overall, the intermediary behaviour under SHI of Al<sub>2</sub>O<sub>3</sub> makes it an interesting case for an original study of the careful description of the modifications and the damaging leading to amorphization at high fluence in the electronic excitation domain. In our study, we have combined the use of an international facility, the ion accelerator GANIL and the IRRSUD beam line, in-situ analysis devices (UV-Visible absorption spectrophotometry at cryogenic temperature and Grazing Incidence X-Ray Diffraction GI-XRD) and ex-situ characterisation (Transmission Electron Microscopy TEM). This paper focusses on the output of a meticulous analysis of the GI-XRD data, as function of fluence and depth, for  $S_e$  higher than the  $S_{eth}$ . To our best knowledge, such detailed analysis on structural and microstructural modifications has not been performed before. These X-Ray diffraction data are confronted with TEM observations of the near surface region and with the colour centre formation in the full range of ion penetration. We show that such experimental combination affords the complete study of point defects, extended defects, structural, microstructural modifications induced by ion irradiation, and energy deposition processes associated to each of these modifications.

## **2. Experimental details**

The investigated Al<sub>2</sub>O<sub>3</sub> samples are polycrystalline pellets prepared by conventional condensed matter processes and commercial (0001) single crystals (500 μm thick, CrysTec GmbH). The high purity commercial Al<sub>2</sub>O<sub>3</sub> powder has been grinded, uniaxially pressed in pellets at 5 bar and sintered at 1300 °C for 6 h. The measured pellet specific mass (2.9 g/cm<sup>3</sup>) is about 70 % of the theoretical one. The irradiation experiments were performed at the IRRSUD beam line of the Grand Accélérateur

National d'Ions Lourds (GANIL) facility in Caen, France. The samples were irradiated at room temperature with 92 MeV  $^{129}\text{Xe}$  ions and 74 MeV  $^{86}\text{Kr}$  ions. The ion flux was kept below  $2 \cdot 10^9 \text{ cm}^{-2} \cdot \text{s}^{-1}$  to prevent macroscopic sample heating. According to the SRIM-2008-04 code [36], and as shown in Fig. 1 for Xe, the main contribution to the energy loss beneath the surface is  $S_e$ , which decreases continuously with increasing penetration depth, unlike the contribution  $S_n$  (represented here also by the dpa) which is mainly observed close to the end of the projected range ( $R_p$ ). The displacement cross section  $\sigma_d$  was obtained using displacement energies of 20 eV for Al and 50 eV for O in the quick Kinchin and Pease option [37] and  $\text{dpa} = \sigma_d \times \Phi$ , with  $\Phi$  being the fluence. The irradiation conditions are rather similar using Xe or Kr, the same parameter evolutions are observed as function of depth for Kr than those for Xe. The electronic stopping power is estimated at the surface to be 21 keV/nm for 92 MeV Xe and ~~to~~ 15.7 keV/nm for 74 MeV Kr. At the implantation peak, the dpa values calculated at  $1 \cdot 10^{14} \text{ ions/cm}^2$  are 0.12 dpa for Xe and 0.085 dpa for Kr, and both projected ranges are rather similar. Note that we performed SRIM calculations with the theoretical density ( $3.98 \text{ g/cm}^3$ ) since in each grain it is the effective density, it is the only way to evaluate the exact electronic stopping power. In this case the experimental penetration depth has to be rescaled (by using SRIM calculations with the experimental density to estimate the rescaling factor). Both depth values, experimental (bottom) and theoretical (top), are drawn in Fig. 1.

To gain time and to avoid influences of variations arising from the target material, in-situ analysis (UV-Vis spectrometry and X-Ray diffraction, without removing the sample from the vacuum chamber) were performed [38,39]. Two modes were used for the in-

situ irradiation: sequential with irradiation and analysis performed at different times, and simultaneous with online analysis when the beam is on.

In-situ optical absorption analysis have been performed on a transparent sample with a device which is composed of a cryogenic head (to cool the sample down to 15 K) and a Varian Cary 300 UV-Visible spectrometer in the 190-900 nm spectral range. Single crystal of (0001)-Al<sub>2</sub>O<sub>3</sub> is used as polycrystalline pellets are not transparent in transmission mode. Irradiation and spectra were done under high vacuum conditions ( $\approx 10^{-8}$  mbar) at normal incidence. A 90° rotation allows switching from the irradiation position to the spectra acquisition position, therefore the sequential mode for irradiation and online analysis takes place for this technique. UV-Vis spectrometry works in transmission geometry with a mask of 2mm×5mm. Besides the irradiated part is probed as well as the non-irradiated one beyond the implantation depth.

To do a depth profile of only damaged slices, see Fig.1, grazing incidence X-Ray diffraction (GI-XRD) at two different incident angles were performed (1° and 2°). The definition of the 0° angle is quite difficult and the estimated error bar on the real value of the incidence angle could reach one degree. The two sequential XRD in-situ measurements were done on two different samples. By using the penetration depth of X-Rays, including the absorption effect in Al<sub>2</sub>O<sub>3</sub>, and taking 90 % of I/I<sub>0</sub> intensity ratio, these incident angles aim to probe depth slices of  $4.5 \pm 5 \mu\text{m}$  at 1° X-Ray incident angle and  $9.4 \pm 5 \mu\text{m}$  at 2°, with error bars considering possible misalignments, density differences and slight parameter fluctuations. The relative intensities of the signal corresponding to the first layer (< 4.5  $\mu\text{m}$ ) and to the buried layer (between 4.5  $\mu\text{m}$  and 9.4  $\mu\text{m}$ ) have been estimated and are reported in table I. We consider in the paper the full slices (0 - 4.5  $\mu\text{m}$ : “thin” and 0 - 9.4  $\mu\text{m}$ : “thick”). A BRUKER D8 Discover

powder diffractometer was used in  $\theta/\theta$  geometry (reflection mode) with a parallel X-Ray beam obtained from a Göbel mirror, for a better control of the incident angle. A Cu anode emitting a  $K_{\alpha 1}$  line at 1.5406 Å and a  $K_{\alpha 2}$  line at 1.5444 Å was employed. A 1D detector (Vantec-1) was used as its energy discrimination can be adjusted close to the Cu radiation energy of the X-Ray diffraction source to minimize the impact of background due to the ion-target interaction [38]. Rietveld refinements have been performed on the diffraction patterns with the Fullprof software package using the Thompson-Cox-Hastings function as profile function for the structural and microstructural analysis [40,41]. For each diffraction condition, the instrumental contribution on the measured spectra has been measured on LaB<sub>6</sub> reference material. The refinements have a sufficient good quality when the agreement factors  $R_F$ ,  $R_B$  are below 5%, and  $\chi^2$  is near to 1, assuming the theoretical rhomboedral  $R\bar{3}c$  symmetry of Al<sub>2</sub>O<sub>3</sub>.

Ex-situ Transmission Electron Microscope (TEM) observations were carried out with a JEOL 2010F electron microscope operating at 200 kV, equipped with a field emission gun. Cross-section (XTEM) specimens were prepared by standard methods: bulk single-crystalline samples were mechanically thinned down to 100 µm, dimpled down to less than 5 µm and finally thinned until perforation by a Gatan Precision Ion Milling System from both sides with 5 keV Ar<sup>+</sup> ions under a 5° incidence angle. Cross-sections on polycrystalline pellets were prepared by focused ion beam with a Helios Nanolab 660 with Ga<sup>+</sup> ions accelerated at 30 keV (decreased down to 2 keV for the final step).

### **3. Results/Discussion**

#### *3.1 Point defect formation*

Point defect formation such as oxygen vacancy formation was characterised by optical absorption. In-situ spectra are represented in Fig. 2 for different Kr fluences. The non-irradiated sample does not exhibit absorption bands, and thus the initial state is free of absorbent defects. In the studied fluence range (up to  $2.5 \cdot 10^{13}$  Kr.cm<sup>-2</sup>), the sample remains crystalline to a very large extent (> 80 %, see section 3.2). This was not systematically the case in some previous work using Swift Heavy Ions [42]. Consequently, in our work, the formation kinetics of optically active point defects is not affected by amorphization. Besides, and contrary to the XRD results obtained in reflection mode at grazing incidence, in-situ absorption is done in transmission mode measuring over the irradiated depth (so with different  $S_e$  and  $S_n$  contributions) as well as the non-irradiated layer of the single crystal. With increasing Kr fluence, the spectra exhibit gradually the formation of four absorption bands related to colour centres similar to those already reported for different irradiation conditions: reactor neutron [43,44], low energy ions [45], or SHI at higher  $S_e$  [16,42,46]. Bands are at approximately 6.05 eV for F centres (oxygen vacancy with two electrons) and 6.3, 5.4 and 4.8 eV for F<sup>+</sup> centres (oxygen vacancy with one electron) [46,47]. The absorption spectra were decomposed into four contributions, corrected by a baseline subtraction, in order to only extract information on the 6.05 eV band for F centres which are, by far, the most formed of the optical active defects. The area density of F centres ( $N_F$  [cm<sup>-2</sup>]) is then determined by using Smakula's formula [48] linking absorption band characteristics and colour centre concentration,

$$N_F = 2 \times 10^{17} \frac{n}{f(n^2+2)^2} \times OD \times W_{1/2} \quad (1)$$

where  $n$  represents the refractive index,  $f$  the oscillator strength of the corresponding transition,  $W_{1/2}$  the width of the absorption band and  $OD$  the optical density at this energy. The values for these parameters used in other studies [16,42,49] for F centres in sapphire are not well harmonized and, in some cases, not understandable. Here, we decided to adopt the oscillator strength suggested by Evans and Stapelbroek [50],  $f$  was theoretically calculated for the one electron centre ( $f = 0.65$  for the  $F^+$  centre) and to supposed be twice for the two electrons centre ( $f = 1.3$  for the F centre), and the refractive index at this wavelength was taken as  $n = 1.9$ . The obtained fluence evolution of  $N_F$  is reported in Fig. 3.

The dynamics of the point defect population is probably complex, as different processes like recombination and cluster formation have to be taken into account [51], by contrast annihilation on the grain surface is excluded as there is no internal surface in single crystals. At such low temperature 15K, point defects are not mobile limiting such complex behaviour. However a simplification is to consider that point defect creation kinetics is ruled by a zero order creation and a first order destruction leading to a saturation of concentration at high fluences (see the fit called “zero and first order” in Fig. 3). As there are evidences in the literature indicating that the oxygen vacancies are created by ballistic events [16], the appropriated parameter is the dpa on the oxygen lattice. The expected evolution of the F centre concentration,  $c_F$ , is given by the differential equation  $(dc_F)/(d dpa) = \varepsilon - \nu c_F$ , a zero order creation and a first order destruction, where  $\varepsilon$  is the creation efficiency and  $\nu$  the atomic recombination volume. Saturation concentration  $c_\infty$  corresponds to  $(dc_F)/(d dpa)=0$  in the case of  $c_\infty = \varepsilon/\nu$ . Then  $c_F = c_\infty (1 - \exp(-\nu dpa))$ . At low fluence (dpa),  $c_F$  evolves linearly:  $c_F = \varepsilon dpa$ . As the measurement integrates the concentration along the ion path, for analysing the

evolution of  $c_F$  with fluence it is necessary to consider the evolution with depth ( $x$ ) of the displacement cross section,  $\sigma_d^o(x)$ , the superscript stands for oxygen displacements. Because  $\sigma_d^o(x)$  value increases with depth (it evolves like the  $S_n$  with depth, see fig 1), saturation occurs earlier at the end of range than at the near surface. Consequently  $N_F$  evolution with fluence cannot be a simple exponential law (fit called “zero and first order” in Fig. 3). To our best knowledge, in previous works, even when  $\sigma_d^o$  varies significantly over the sample thickness this variation has not been systematically considered by analysing the fluence evolution of  $N_F$ . For the evolution with depth of  $\sigma_d^o$ , we have calculated  $\sigma_d$  as described in §2 (Fig. 1) and have multiplied this quantity by the mean fraction of O vacancies among the total displacements, estimated by using SRIM in full cascade approximation.

With these approximations:

$$N_F = N \frac{\varepsilon}{\nu} \int_0^{x_{max}} \left(1 - \exp(-\nu \sigma_d^o(x) \Phi)\right) dx \quad (2)$$

Where  $N$  is the atomic density and  $x_{max}$  the depth where no more displacements are induced. The best fit of the data using Eq. 2 is presented in Fig. 3 by the fit called “model Eq. 2”. This equation perfectly fits the data indicating that considering an evolution of  $c_F$  with a zero order creation and a first order destruction is enough to describe the F centre population evolution with fluence. The fit has two free parameters,  $\varepsilon$  and  $\nu$ . The best fit is obtained when  $\nu = 572 \text{ at}^{-1}$  and  $\varepsilon = 14 \%$  meaning that around 14 % of the total displaced atoms (corresponding to 40 % of the displaced oxygen atoms), generated by 74 MeV Kr ions create stable F centres.

Even when the point defect creation is triggered by ballistic events,  $S_e$  could eventually change the point defect creation efficiency  $\varepsilon$ . For instance, in III-Nitrides, coupled

effects of  $S_e$  and  $S_n$  are huge for colour centre formation in AlN but not in GaN [39]. Besides, in  $Al_2O_3$ , recovery of point defects induced by ballistic events due to a subsequent irradiation in the electronic stopping regime has been reported [52]. Data published in the literature correspond to very different irradiation conditions in terms of  $S_e$  and ENSP (electronic on nuclear stopping power ratio). For instance, irradiations with energies typical of implantation (some tens of keV to some hundreds of keV) for ions ranging from H to Kr are reported in [4,45,49,52], few MeV ion irradiations were also performed as well as Swift Heavy Ion Irradiations [16,19,42,46,53] (with data up to the maximum  $S_e$  reachable with monoatomic projectiles (2.64 GeV U [54]). In addition to these ion irradiations, data issued from neutron irradiations are also available [43,44]. In practice, literature results more or less cover the full range of possible  $S_e$  and ENSP. It is then worth trying to detect an influence of  $S_e$  on  $\varepsilon$  in the present  $Al_2O_3$  case. Unfortunately, the available data are fragmented, and even when harmonising the results (same parameters in Eq. 1, same calculation of  $\sigma_d^o$ , use of Eq. 2 when necessary and considering the irradiation cases where samples remain mainly crystalline) one leads to relative dispersed values for  $\varepsilon$  and  $\nu$ , without any straightforward influence of  $S_e$ . For the moment, and waiting for systematic studies on the role of  $S_e$  and ENSP, one can only conclude, that in sapphire some percent up to few tens of percent of the displaced atoms generate stable F centres whatever the initial conditions, *i. e.* the energy and the nature of the projectile that means the  $S_e$ , ENSP and average Primary Knock-on Atom (PKA) energy. Moreover the fact that the data can be better fitted when taking into account the evolution of  $\sigma_d^O$  with depth indicates that  $S_n$  is the crucial factor for F centre formation.

### 3.2 Phase transition kinetics

Fig. 4 shows XRD patterns recorded in-situ during 92 MeV Xe irradiation (4 fluences are shown) in sequential mode at the two grazing incident angles. The non-irradiated patterns are characteristic of high quality powder samples, all Bragg reflections corresponding to the  $\alpha$ -phase of  $\text{Al}_2\text{O}_3$  structure (space group  $R\bar{3}c$  n°167) are present without any parasitic reflection and without any indication of polycrystalline texture.

With the fluence increase, the patterns show a decrease of the overall diffracted intensity in the thick slice (probed by XRD measurement with an incidence angle of  $2^\circ$ ), and until almost complete reflexion extinction in the thin slice (probed by the measurement at  $1^\circ$ ). This intensity reduction is associated to the increase of diffuse scattering around  $2\Theta = (22-35)^\circ$ . This reveals a progressive phase transition from a  $R\bar{3}c$  crystalline structure with more and more defective structure (peak broadening, shifting,...) to an amorphous phase, the final state of the thin slice being almost fully amorphous. For the thick slice, the transition is following the same evolution, however it does not reach the fully amorphous state. Neither preferential orientation nor texture obtained from the structural refinement is observed with the fluence increase as the relative intensities of all reflections are consistent with a reference pattern of  $\alpha\text{-Al}_2\text{O}_3$  powder. Therefore there is no other concurrent effect than damage production and amorphization contributing to the decrease of the global diffracted intensity. To quantify the phase evolution with the ion fluence, the amorphization fraction is extracted from the ratio between irradiated and virgin data for two values: the net area of (113) Bragg reflection (all reflection evolve much in the same way) and the scale factor estimated in Rietveld refinement. The scale factor is generally used to adjust the relative contribution of individual phases to the overall diffraction pattern allowing quantitative analysis. As in our case there is only one diffracting phase and the other is the amorphous one, the

loss of scale factor corresponds to amorphization. Fig. 5 shows the evolution of the amorphous ratio in the thick (Fig. 5a) and thin (Fig. 5b) slices as function of the Xe fluence. The simultaneous mode used during the in-situ experiment (grey dots on Fig. 5) is much more accurate compared to the sequential one (black dots on Fig. 5) regarding the number of points, 200 against 12, for drawing kinetics as discussed in Grygiel *et al.* [38]. At high fluence ( $0.8 \cdot 10^{14}$  Xe/cm<sup>2</sup>) we estimate that there is a saturation of the amorphized fraction to 90% in the thin slice while only 60% is reached in the thicker one. Observations by XTEM (Fig. 6a) on the irradiated pellet at  $8 \cdot 10^{13}$  cm<sup>-2</sup>, the maximum fluence for pellets, indicate that the material is fully amorphous on the first 4  $\mu$ m (see diffraction pattern Fig. 6d). Deeper than this amorphous layer, a 2-3  $\mu$ m thick layer is visible with a high concentration of defects and partially amorphous grains. In Fig. 6c, the amorphous shell is visible and the dark contrasts inside the grain are due to small clusters of defect, but the crystallinity remains. No clear modification is evidenced beyond 7  $\mu$ m in depth (see Fig. 6b). Considering the porosity, a layer of 4  $\mu$ m is equivalent to a layer of 2.8  $\mu$ m of Al<sub>2</sub>O<sub>3</sub> with the theoretical density. This is more than reported in experiments performed in similar conditions (85 MeV I,  $S_e \approx 20$  keV/nm) by Aruga *et al.* [18] giving 2  $\mu$ m of amorphous phase for polycrystals irradiated at a three times higher fluence ( $2.8 \cdot 10^{14}$  ions/cm<sup>2</sup>), considering that there is no initial porosity in the samples of Aruga *et al.*, their density is the theoretical one. Observations by XTEM of (0001)-Al<sub>2</sub>O<sub>3</sub> irradiated by 92 MeV Xe at  $2 \cdot 10^{14}$  ions.cm<sup>-2</sup> show an amorphous layer of 500 nm and a crystalline layer beyond with lot of black dots due to formation of defects during irradiation (Fig. 6e). As a conclusion, the initial grain size (of any kind: single-crystalline or polycrystalline with 370 nm, as here, or more than 1  $\mu$ m, as in the Aruga experiment [18]) plays an important effect on the kinetics of amorphization,

slower is the amorphization as the crystallite size increases. Indeed an amorphous front line grows from the surface into the material, but also across grain boundaries or at the grain surface, amorphization velocity is faster when samples are poly-crystalline and exhibit grain boundaries [18, 24]. Amorphization kinetics is then sensitive to internal surfaces.

The transition kinetics (shown in Fig. 5) allows the analysis of defect creation mechanisms. The model of ion impact overlapping described by Gibbons [5] is used to fit the experimental curves and to understand if single or multiple impacts are necessary for amorphization. As observed for Xe irradiation in Fig. 5a and 5b, a better agreement is obtained for multiple impacts, especially in the high fluence region, compared to the single impact fit. These fits induce, for the double impact, a damaged cross section with a diameter of  $5.0 \pm 0.8$  nm in the thin slice and  $4.0 \pm 1.0$  nm in the thick slice. Similar simultaneous experiments for 74 MeV Kr irradiation (Fig. 5c) have also led to a double impact kinetics, slower in fluence, with a smaller damage cross section of  $2.2 \pm 0.4$  nm diameter in the thin slice, consistent with the lower  $S_e$  of the Kr beam (still above  $S_{eth}$  for amorphization). These fits show that the amorphization process of  $Al_2O_3$  is not a direct amorphization under SHI irradiation at around a hundred MeV. An accumulation of few impacts is highlighted to reach the high fluence steady state. This is consistent with literature results obtained by TEM which evidenced that a single track stays crystalline but with disorder and density variation in the core included in a diameter of 4 nm of a cylinder-like disordered region [25,30]. The description of the amorphization process might be more complicated than the classical overlap model as it was also shown that amorphization in  $Al_2O_3$  takes place at the surface and is influenced by possible internal surfaces. Thus, perhaps, the given cross section is an average over the

one of the first impact (pre-damaged cylinder) and the one of the subsequent amorphization, which might not be exactly equal.

### *3.3 Modifications of the crystalline matrix*

Formation of defects (point and extended defects) cause either long range lattice expansion, swelling due to their additional volume and short range heterogeneous lattice distortion to accommodate locally, around defect volume, the slight displacement of atoms from their crystallographic sites. In order to get more information on the lattice distortion and on other structural modifications due to irradiation as well as microstructural evolution, we performed Rietveld refinements on the diffracted patterns.

#### *i) Microstructural modifications: microstrain and domain size evolution*

The Fig. 7 shows the results of microstructural analysis performed in the thick slice by Rietveld refinement. The microstructural analysis is based on the analysis of the width and shape of the Bragg reflections. The instrumental contribution (§2) is taken into account and is constant for different fluences. Two broadening contributions are considered: the size of the coherent diffraction domains with a Lorentzian contribution and the microstrain with a Gaussian contribution. We did not consider a size distribution, but only a mean value. The evolutions of coherent domain size and microstrain as function of ion fluence are shown in Fig. 7.

An evolution with the fluence is observed for the microstrain, being the local fluctuations of interreticular d-spacing induced by defect creation. A large increase is noticed at low fluence up to saturation around 2 to  $4 \cdot 10^{13}$  Xe/cm<sup>2</sup> corresponding to a

content of the amorphous phase above 40-60 %. This fluence behaviour is well described by a Poisson law (single impact model) inducing a damage cross section of  $4.0 \pm 1.0$  nm of diameter which is the same as the amorphization cross section (but with a kinetics driven by multiple impacts). Then microstrain appearance is linked to the first passage of ions and microstrain is certainly present in the core, the shell and the surrounding parts, more or less extended, of the ion track. The observation of latent tracks and matrix has been done on a cross section on a large grain, i.e. single crystal, and is shown in Fig. 8. The sample is irradiated in the regime of single impacts,  $2 \cdot 10^{11}$  Xe/cm<sup>2</sup>, where track overlapping is very limited. Discontinuous tracks are observed on Fig. 8, the dark contrasts around these discontinuous strings correspond to a small strain field around the ion path, indicating that at low fluence disordered tracks induce microstrain and strain fields in the track region. A description by HRTEM and MD simulation of the strain field around tracks was recently published by O'Connell *et al.* [30] indicating that an underdense core inducing strain is surrounded by an overdense shell.

Beside the contribution to peak broadening of microstrain, Fig. 7 shows also the irradiation effect on the coherent domain size. The virgin isotropic domain size is estimated to  $370 \pm 30$  nm which is consistent with the grain size measured in TEM images, the pristine grain size is still measurable after irradiation, as shown Fig. 6a beyond 7  $\mu$ m of thickness. Under irradiation, a size decrease of coherent diffracting domains takes place with the fluence increase which is estimated around 70 % in the irradiated crystals from X-Ray data. This evolution evolves faster and saturates earlier with the fluence (around  $1 \cdot 10^{13}$  cm<sup>-2</sup>) than amorphization (and even a little more than microstrain). Moreover, if we assume that the change in size exclusively stems from a

partial amorphization of grains, it would lead to a much higher amorphous fraction than experimentally observed (*i. e.* at  $2 \cdot 10^{13} \text{ cm}^{-2}$ , the decrease in size is of 80 % and the amorphous fraction is 35 %). Indeed the relation between crystallite size decrease and the amorphous fraction depends how amorphization occurs. For instance, considering that grains are spheres and that amorphization occurs at the grain surface, 50 % in size decrease corresponds to an amorphous fraction of 87.5 %. This last value could be smaller for other topologies, but such a small relative change in size must induce a much higher change in amorphous fraction than the one experimentally estimated.

XTEM observations, see Fig. 9, indicate that there is an amorphization of grains starting at the grain boundary (or at the grain surface as the porosity is important), with grains composed of a shell of amorphous phase and a crystalline core more or less defective (see Fig. 9c) in the intermediate zone (between 4 and 7  $\mu\text{m}$  in depth), as already observed Fig. 6c. The thickness of the shell depends on the depth (maximum shell at 4  $\mu\text{m}$ ) but also differ from a grain to another (at the same depth), perhaps due to the initial difference in size and shape. Then an inaccuracy in the size calculation by XRD can be done considering a uniform shape, which is apparently not the case (as seen in the intermediate area 4 -7  $\mu\text{m}$  and above 7 $\mu\text{m}$ ). Indeed in Fig. 6a, Fig. 6c, Fig. 9a and Fig. 9b, variation in grain size and grain shape are observed as function of depth and even at the same depth. In each grain of the intermediate area it appears very small crystalline domains embedded in a nearly amorphous matrix. In these disordered areas (Fig. 9b), in one grain we observe different contrast variations in the image highlighting the appearance of small crystalline domains slightly disorientated as shown by the broadening of the diffraction spot into extended spot or even split spots. However the apparition of disorientated domains (estimated at maximum  $\pm 6^\circ$  on the diffraction

pattern), is too small (in terms of volume and disorientation level) to be quantified macroscopically as neither texture nor preferential orientation is extracted from Rietveld refinements (see paragraph 3.2). This formation of small crystalline domains slightly disorientated is like grain subdivision and these small crystalline areas have an influence on the broadening of X-Ray reflections. Thus as a function of fluence, a comparison between X-Ray data (mean coherent size) and TEM observations are tricky in terms of absolute values even if they exhibit the same trend of decrease and are in agreement with the initial grain size. All of this leads us to conclude that another phenomenon than amorphization contributes to the crystallite size decrease, and that could be grain subdivision. Under SHI irradiation, for various oxides, grain fragmentation is commonly reported [55-58] and at the difference of special case fluorite oxides where a grain growth is observed [59-61]. However only sparse data are currently found for Al<sub>2</sub>O<sub>3</sub> irradiated with SHI. Aruga *et al.* [18] have reported, for polycrystalline Al<sub>2</sub>O<sub>3</sub> with large grains (few hundred nanometers), the TEM observation of splitting, polygonization, rotation and displacement effects of the grains after irradiation with 85 MeV iodine. Skuratov *et al.* [20] have pointed out for single crystals by TEM the presence of subgrains of about 200 nm sizes after the 710 MeV Bi irradiation. Klaumünzer *et al.* [62] have shown by HR-XRD on single crystals a grain size decrease down to nanocrystals and their grain rotation under 945 MeV Au. Consequently grain subdivision could be a general effect for Al<sub>2</sub>O<sub>3</sub> under SHI irradiation whatever the initial grain size.

*ii) Atomic positions*

Continuing with the analysis of the modification on the crystalline part of the sample, Fig. 10 shows the variations of the atomic coordinates,  $z$  of the aluminium and  $x$  of the

oxygen, extracted from Rietveld refinements for patterns recorded at  $2^\circ$  of incidence, in the thick slice, as function of the Xe fluence.

With the space group  $R\bar{3}c$  (hexagonal axes), the aluminium Wyckoff position is 12c (0, 0, z) with the virgin value  $z_0 = 0.352$  and the oxygen Wyckoff position is 18e (x, 0, 0.25) with  $x_0 = 0.12$ . Both evolve when the fluence increases and lead to modifications of the unit-cell arrangement, however a larger variation is observed for the oxygen which is thus more largely displaced by irradiation than the aluminium. This is consistent with anion-selective defect processes observed by RBS [22,26], for which the anionic lattice was more sensitive to disorder induced by irradiation, with a disorder cross section twice higher than the one of aluminium.

### *iii) Volume expansion*

The unit-cell parameters and unit-cell volume have also been extracted from Rietveld refinements for each fluence and slice. Slight anisotropic expansions of  $c$  and  $a$  are observed with the fluence increase. The evolution with fluence is fast as above  $1 \cdot 10^{13}$   $\text{cm}^{-2}$  a clear saturation is observed. The  $c$  maximum expansion is slightly higher than the expansion in  $a$ . At  $1 \cdot 10^{13}$  ions/ $\text{cm}^2$ , the maximum strain is  $0.25 \pm 0.01$  % for  $c$  and  $0.20 \pm 0.01$  % for  $a$  in the thick slice against  $0.23 \pm 0.01$  % and  $0.14 \pm 0.01$  % in the thin slice for  $c$  and  $a$ , respectively. Remember that at  $1 \cdot 10^{13}$  ions/ $\text{cm}^2$ , the ratio of amorphous phase is around 20% in the thick slice compared to 50% in the thin slice, the amorphization kinetics being by multiple overlaps, the unit-cell parameter evolution is then faster than amorphization. This parameter expansion induces an overall lattice expansion as shown in Fig. 11. Indeed, swelling increases at low fluence before

reaching a maximum value at  $1 \cdot 10^{13}$  Xe/cm<sup>2</sup> and then slightly decreases at high fluence. This volume expansion shows a maximum variation of 0.5 % (at  $1 \cdot 10^{13}$  Xe/cm<sup>2</sup>) in the thin slice against a maximum expansion of 0.7 % in the thick slice. The unit cell swelling is attributed to disordering with octahedron distortions and defect creation. The octahedron distortion is a consequence of the shift of the atoms from their initial crystallographic site (but still participating to diffraction) and of the lattice parameter increase. Thus the inter-atomic distance is changed as well as the angles, the coordination polyhedra are modified, and the unit-cell volume increased. The defects created by irradiation are not any more diffracting atoms as localized outside their Wyckoff positions. This induces disordering of the atom stacking and therefore this induces also unit-cell swelling. At high fluence, a decrease of the swelling and even a compression are observed. This is when amorphization, taking place by the surface with a front line going into the material and across grain boundaries or at the grain surface, reaches important levels (at  $2 \cdot 10^{13}$  Xe/cm<sup>2</sup>, around 80 % amorphous in the thin slice and 50 % in the thick slice). This might constrain crystalline areas and, associated to saturation of point defect concentration, this might induce the high fluence decrease.

Looking at swelling values in literature, lattice swelling extracted from X-Ray diffraction is lower than those extracted from macroscopic dimensional variations. Generally speaking, introduction of only Frenkel pairs should equally affect lattice parameter and volume, inducing swelling by different relaxation around vacancies and interstitials [63]. This equality between changes in lattice parameter and volume no longer takes place when point defect clusters and resulting dislocation loops are formed. Moreover, in more complex irradiation situations, as it is the case here, contributions of

amorphous phase, grain boundary evolution, bubble creation, etc, can lead to a much higher macroscopic swelling up to some percent.

The energy deposition processes at the origin of lattice swelling are relevant to look at, as it is a crossing parameter linked to all the structural variations.

In our experiment, the  $\Delta V/V$  value (around 0.5% for  $1 \cdot 10^{13} \text{Xe/cm}^2$  corresponding to  $3 \cdot 10^{-3}$  dpa at maximum), is around two orders of magnitude higher at same dpa value than  $\Delta V/V$  values given in the literature for low energy irradiation inducing only ballistic collisions where typically  $\Delta V/V$  is one percent per dpa [64]. Thus only  $S_n$  effects cannot explain the observed swelling.

If only  $S_e$  effects would be at the origin of swelling, swelling in the thick slice would be smaller than in the thin slice as  $S_e$  values are maximum at the surface and decrease with depth increase, but we observed the contrary, so only  $S_e$  effects cannot explain the observed swelling.

Thus we believe that a complex effect of both  $S_e$  and  $S_n$  induces the behaviour of swelling as function of depth and fluence, at least at low fluence when amorphization is negligible and dpa small. In the literature, the ENSP is often used to describe microstructure evolution in terms of point defects evolving into dislocation loops [4,8,65]. Indeed these features become increasingly unfavourable with ENSP increase, as loop density decreases whereas loop size increases. In our experiments at high  $S_e$ , electronic excitations play both roles of defect annealing and structural modifications, certainly in the first track, which is not yet amorphous, inducing part of the lattice expansion. Only after track overlap and multiple impacts, electronic excitations play for amorphization. So at low fluence, lattice swelling is not correlated to amorphization. Considering that ENSP may play a role in the first track, as function of depth it evolves

from 130 at surface to 35 at the thin slice limit and down to 2 at the thick slice limit. So on contrary to colour centres created by  $S_n$  or amorphization by  $S_e$ , the swelling of the lattice is due to a complex combination of different phenomenon (point defect creation, dislocation loop formation, lattice distortion due to ion track, effect of the amorphous part of the matrix,...) depending on  $S_e$ ,  $S_n$  or both.

#### 4. Conclusions

Polycrystalline and single-crystalline samples of  $\alpha$ - $\text{Al}_2\text{O}_3$  have been irradiated at the IRRSUD beamline of the GANIL facility by using ion beams inducing intense electronic excitations with  $S_e$  values higher than the  $S_{eth}$  for high fluence amorphization. It has been demonstrated using in-situ (UV-Vis absorption, GI-XRD) and ex-situ techniques (TEM) that  $\text{Al}_2\text{O}_3$  exhibits sensitivity to radiation, in agreement with former literature results, with defect formation and strong modifications of the crystalline lattice. By increasing the ion fluence a progressive phase transition is observed with a multiple impact process from crystalline to amorphous state. The intermediate case of  $\text{Al}_2\text{O}_3$  between a direct amorphizable material and a non amorphizable one promotes structural and microstructural modifications associated to point and extended defects. Indeed, the crystalline matrix exhibits with the fluence an increase of the unit-cell parameters thus a lattice swelling, an increase of microstrain and a shift of oxygen coordinates. Formations of either point or extended defects oblige the matrix to accommodate atomic disorder and extra-volume by long-range and short-range strains. As often in oxides, the oxygen sublattice subject to disorder drives the material behaviour. Further characterisations by energy filtered TEM of the atomic coordination

evolution in the defective region will be performed in the future to study carefully cation and anion selective defects, defect aggregation and accumulation induced by the ion irradiation and their possible correlation to the microstructure evolution. Beside the structural effects, the microstructure of  $\text{Al}_2\text{O}_3$  samples is also affected in this MeV energy range with domain size decrease and amorphization beneath the surface. Moreover from the depth profile, we observed different variations of the former parameters with material depth and consequently energy deposition processes. Then, amorphization requires  $S_e$  values above  $S_{\text{eth}}$ , lattice swelling evolves with combination of both  $S_e$ ,  $S_n$  and point defects are predominant with atomic displacements or  $S_n$ . This study highlights the relationship between energy losses of projectiles into a crystalline matrix and the matrix response. This opens the routes for systematic studies using depth profile and the combination of in-situ and ex-situ techniques, thus to control the defect introduction and to tailor the material properties used under real-world conditions.

## **ACKNOWLEDGMENTS**

The experiments were performed at the IRRSUD beamline of the Grand Accélérateur National d'Ions Lourds (GANIL), Caen, France. The authors thank the CIMAP staff, the CIRIL platform staff, the GANIL technical staff and the overall administrative staff. The authors would like to thank S. Klaumünzer and M. Toulemonde for interesting discussions. This work was partially supported by the ANR funding ALIX-Mai ANR-06-BLAN-0292-01, by the ANR funding “Investissements d’avenir” ANR-11-EQPX-0020, the FEDER and by the Region Basse-Normandie.

## REFERENCES

- [1] K.W. Bladh, R.A. Bideaux, E. Anthony-Morton, and B.G. Nichols, *The Handbook of Mineralogy III*, Mineral Data Publishing, 1997.
- [2] B.M. Berman, M.L. Bleiberg, W. Yeniscavich, Fission fragment damage to crystal structures, *J. Nucl. Mater.* 2 (1960) 129-140.
- [3] C.W. White, C.J. McHargue, P.S. Sklad, L.A. Boatner, G.C. Farlow, Ion Implantation and annealing of crystalline oxides, *Mater. Sci. Rep.* 4 (1989) 41-146.
- [4] S.J. Zinkle, C. Kinoshita, Defect production in ceramics, *J. Nucl. Mater.* 251 (1997) 200-217.
- [5] J. F. Gibbons, Ion implantation in semiconductors – Part II: Damage production and annealing, *Proc. IEEE* 60 (1972) 1062-1096.
- [6] J. Lian, L. Wang, J. Chen, K. Sun, R.C. Ewing, J. Matt Farmer, L.A. Boatner, The order–disorder transition in ion-irradiated pyrochlore, *Acta Mater.* 51 (2003) 1493-1502.
- [7] W.J. Weber, Models and mechanisms of irradiation-induced amorphization in ceramics, *Nucl. Instr. and Meth. B* 166 (2000) 98-106.
- [8] S.J. Zinkle, Effect of irradiation spectrum on the microstructural evolution in ceramic insulators, *J. Nucl. Mater.* 219 (1995) 113-127.
- [9] F.W. Clinard Jr., G.F. Hurley, L.W. Hobbs, Neutron irradiation damage in MgO, Al<sub>2</sub>O<sub>3</sub> and MgAl<sub>2</sub>O<sub>4</sub> ceramics, *J. Nucl. Mater.* 108 (1992) 655-670.
- [10] C. Kinoshita, K. Fukumoto, K. Fukuda, F.A. Garner, G.W. Hollenberg, Why is magnesia spinel a radiation-resistant material?, *J. Nucl. Mater.* 219 (1995) 143-151.
- [11] S.J. Zinkle, G.P. Pells, Microstructure of Al<sub>2</sub>O<sub>3</sub> and MgAl<sub>2</sub>O<sub>4</sub> irradiated at low temperatures, *J. Nucl. Mater.* 253 (1998) 120-132.
- [12] Y. Sina, M. Ishimaru, C.J. McHargue, E. Alves, K.E. Sickafus, Ion beam induced epitaxial crystallization of  $\alpha$ -Al<sub>2</sub>O<sub>3</sub> at room temperature, *Nucl. Instr. and Meth. B* 321 (2014) 8-13.
- [13] M. Toulemonde, S. Bouffard, and F. Studer, Swift heavy ions in insulating and conducting oxides: tracks and physical properties, *Nucl. Instr. and Meth. B* 91 (1994) 108-123.
- [14] G. Sattonnay, C. Grygiel, I. Monnet, C. Legros, M. Herbst-Ghysel, L. Thomé, Phenomenological model for the formation of heterogeneous tracks in pyrochlores irradiated with swift heavy ions, *Acta Mater.* 60 (2012) 22-34.
- [15] W. Jiang, R. Devanathan, C.J. Sundgren, M. Ishimaru, K. Sato, T. Varga, S. Manandhar, A. Benyagoub, Ion tracks and microstructures in barium titanate irradiated with swift heavy ions: A combined experimental and computational study, *Acta Mater.* 61 (2013) 7904-7916.
- [16] B. Canut, A. Benyagoub, G. Marest, A. Meftah, N. Moncoffre, S. M. M. Ramos, F. Studer, P. Thevenard, M. Toulemonde, Swift-uranium-ion-induced damage in sapphire, *Phys. Rev. B* 51 (1995) 12194-12201.
- [17] S.M.M. Ramos, N. Bonardi, B. Canut, S. Bouffard, S. Della-Negra, Damage creation in  $\alpha$ -Al<sub>2</sub>O<sub>3</sub> by MeV fullerene impacts, *Nucl. Instr. and Meth. B* 143 (1998) 319-332.
- [18] T. Aruga, Y. Katano, T. Ohmichi, S. Okayasu, Y. Kazumata, Amorphization behaviors in polycrystalline alumina irradiated with energetic iodine ions, *Nucl. Instr. and Meth. B* 166 (2000) 913-919.

- [19] T. Mohanty, N.C. Mishra, F. Singh, U. Tiwari, D. Kanjilal, Swift heavy ion irradiation induced modifications in sapphire, *Nucl. Instrum. Methods B* 212 (2003) 179-183.
- [20] V.A. Skuratov, S.J. Zinkle, A.E. Efimov, K. Havancsak, Swift heavy ion-induced modification of Al<sub>2</sub>O<sub>3</sub> and MgO surfaces, *Nucl. Instr. and Meth. B* 203 (2003) 136-140.
- [21] G. Szenes, Ion-induced amorphization in ceramic materials, *J. Nucl. Mater.* 336 (2005) 81-89.
- [22] A. Kabir, A. Meftah, J. P. Stoquert, M. Toulemonde, I. Monnet, Amorphization of sapphire induced by swift heavy ions: A two step process, *Nucl. Instr. and Meth. B* 266 (2008) 2976-2980.
- [23] K.R. Nagabhushana, B.N. Lakshminarasappa, F. Singh, Photoluminescence and Raman studies in swift heavy ion irradiated polycrystalline aluminum oxide, *Bull. Mater. Sci.* 32 (2009) 515-519.
- [24] N. Okubo, N. Ishikawa, M. Sataka, S. Jitsukawa, Surface amorphization in Al<sub>2</sub>O<sub>3</sub> induced by swift heavy ion irradiation, *Nucl. Instrum. Methods B* 314 (2013) 208-210.
- [25] V. A. Skuratov, J. O'Connell, N. S. Kirilkin, J. Neethling, On the threshold of damage formation in aluminum oxide via electronic excitations, *Nucl. Instr. and Meth. B* 326 (2014) 223-227.
- [26] A. Kabir, A. Meftah, J. P. Stoquert, M. Toulemonde, I. Monnet, M. Izerrouken, Structural disorder in sapphire induced by 90.3 MeV xenon ions, *Nucl. Instr. and Meth. B* 268 (2010) 3195-3198.
- [27] N. Khalfaoui, J.P. Stoquert, F. Haas, C. Traumann, A. Meftah, M. Toulemonde, Damage creation threshold of Al<sub>2</sub>O<sub>3</sub> under swift heavy ion irradiation, *Nucl. Instr. and Meth. B* 286 (2012) 247-253.
- [28] S. Klaumünzer, M. Bender, A. Romanenko, D. Severin, Ion-beam-induced stresses in polycrystalline  $\alpha$ -alumina, GSI Report 2015-1 (2015) 259, APPA-MML-MR-07.
- [29] H. Zirour, M. Izerrouken, A. Sari, Radiation damage induced in Al<sub>2</sub>O<sub>3</sub> single crystal by 90 MeV Xe ions, *Nucl. Instr. and Meth. B* 365 (2015) 269-272.
- [30] J.H. O'Connell, R.A. Rymzhanov, V.A. Skuratov, A.E. Volkov, N.S. Kirilkin, Latent tracks and associated strain in Al<sub>2</sub>O<sub>3</sub> irradiated with swift heavy ions, *Nucl. Instrum. Methods B* 374 (2016) 97-101.
- [31] P.N. Terekhin, R.A. Rymzhanov, S.A. Gorbunov, N.A. Medvedev, A.E. Volkov, Effect of valence holes on swift heavy ion track formation in Al<sub>2</sub>O<sub>3</sub>, *Nucl. Instr. and Meth. B* 354 (2015) 200-204.
- [32] A. Meftah, F. Brisard, J. M. Costantini, M. Hage-Ali, J. P. Stoquert, F. Studer, M. Toulemonde, Swift heavy ions in magnetic insulators: A damage-cross-section velocity effect, *PRB* 48 (1993) 920-925.
- [33] Y. Y. Wang, C. Grygiel, C. Dufour, J. R. Sun, Z. G. Wang, Y. T. Zhao, G. Q. Xiao, R. Cheng, X. M. Zhou, J. R. Ren, S. D. Liu, Y. Lei, Y. B. Sun, R. Ritter, E. Gruber, A. Cassimi, I. Monnet, S. Bouffard, F. Aumayr, M. Toulemonde, Energy deposition by heavy ions: Additivity of kinetic and potential energy contributions in hillock formation on CaF<sub>2</sub>, *Sci. Rep.* 4 (2014) 5742-6p.
- [34] M. Sall, I. Monnet, F. Moisy, C. Grygiel, S. Jublot-Leclerc, S. Della Negra, M. Toulemonde, E. Balanzat, Track formation in III-N semiconductors irradiated by swift heavy ions and fullerene and re-evaluation of the inelastic thermal spike model, *J. of Mater. Sci.* 50 (2015) 5214-5227.

- [35] W.J. Weber, E. Zarkadoula, O.H. Pakarinen, R. Sachan, M.F. Chisholm, P. Liu, H. Xue, K. Jin, Y. Zhang, Synergy of elastic and inelastic energy loss on ion track formation in SrTiO<sub>3</sub>, *Sci. Rep.* 5 (2015) 7726-6p.
- [36] J. P. Biersack, L. G. Haggmark, A Monte Carlo computer program for the transport of energetic ions in amorphous targets, *Nucl. Instrum. and Meth.* 174 (1980) 257-269.
- [37] R.E. Stoller, M.B. Toloczko, G.S. Was, A.G. Certain, S. Dwaraknath, F.A. Garner, On the use of SRIM for computing radiation damage exposure, *Nucl. Instr. and Meth. B* 310 (2013) 75-80.
- [38] C. Grygiel, H. Lebius, S. Bouffard, A. Quentin, J. M. Ramillon, T. Madi, S. Guillous, T. Been, P. Guinement, D. Lelièvre, I. Monnet, Online in situ x-ray diffraction setup for structural modification studies during swift heavy ion irradiation, *Rev. Sci. Instrum.* 83 (2012) 013902-6p.
- [39] M. Sall, I. Monnet, C. Grygiel, B. Ban d'Etat, H. Lebius, S. Leclerc, E. Balanzat, Synergy between electronic and nuclear energy losses for color center creation in AlN, *EPL* 102 (2013) 26002-5p.
- [40] J. B. Hastings, W. Thomlinson, D. E. Cox, Synchrotron X-ray Powder Diffraction, *J. Appl. Cryst.* 17 (1984) 85-95.
- [41] J. Rodriguez-Carvajal, Recent advances in magnetic structure determination by neutron powder diffraction, *Physica B* 192 (1993) 55-69.
- [42] A. Kabir, A. Meftah, J. P. Stoquert, M. Toulemonde, I. Monnet, Defects creation in sapphire by swift heavy ions: A fluence depending process, *Nucl. Instr. and Meth. B* 267 (2009) 957-959.
- [43] K. Tanimura, N. Itoh, F.W. Clinard, Volume change of Al<sub>2</sub>O<sub>3</sub> and MgAl<sub>2</sub>O<sub>4</sub> induced by 14-MeV neutron irradiation, *J. Nucl. Mater.* 150 (1987) 182-185.
- [44] M. Izzerouken, A. Meftah, S. Berkani, Thermoluminescence study of Al<sub>2</sub>O<sub>3</sub> and Y<sub>3</sub>Al<sub>5</sub>O<sub>12</sub> single crystals irradiated with reactor neutrons, *Nucl. Instr. and Meth. B* 326 (2014) 90-94.
- [45] P. Agnew, Displacement damage efficiency in sapphire, *Nucl. Instr. and Meth. B* 65 (1992) 305-310.
- [46] B. Canut, S.M.M. Ramos, P. Thevenard, N. Moncoffre, A. Benyagoub, G. Marest, A. Meftah, M. Toulemonde, F. Studer, High energy heavy ion irradiation effects in  $\alpha$ -Al<sub>2</sub>O<sub>3</sub>, *Nucl. Instrum. Methods B* 80 (1993) 1114-1118.
- [47] M. L. Dalal, M. Rahmani, P. D. Townsend, UV absorption of ion implanted sapphire, *Nucl. Instr. and Meth. B* 32 (1988) 61-65.
- [48] A. Smakula, Über Erregung und Entfärbung lichtelektrisch leitender alkalihalogenide, *Z. Phys.* 59 (1930) 603-614.
- [49] E.N. Epie, D.N. Wijesundera, B.P. Tilakaratne, Q.Y. Chen, W.K. Chu, Rate of F center formation in sapphire under low-energy low-fluence Ar<sup>+</sup> irradiation, *Nucl. Instr. and Meth. B* 371 (2016) 303-306.
- [50] B. D. Evans, M. Stapelbroek, Optical properties of the F<sup>+</sup> center in crystalline Al<sub>2</sub>O<sub>3</sub>, *Phys. Rev. B* 18 (1978) 7089-7098.
- [51] K. Moritani, Y. Teraoka, I. Takagi, M. Akiyoshi, H. Moriyama, Production and reaction kinetics of radiation-induced defects in  $\alpha$ -alumina and sapphire under ion beam irradiation, *J. Nucl. Mater.* 373 (2008) 157-163.
- [52] G. W. Arnold, G.B. Krefft, C. B. Norris, Atomic displacement and ionization effects on the optical absorption and structural properties of ion-implanted Al<sub>2</sub>O<sub>3</sub>, *Appl. Phys. Lett.* 25 (1974) 540-542.

- [53] T. Mohanty, N.C. Mishra, F. Singh, S.V. Bhat, D. Kanjilal, Color center formation in sapphire by swift heavy ion irradiation, *Rad. Meas.* 36 (2003) 723-727.
- [54] Y. Song, Q. Liu, Y. Sun, J. Liu, Z. Zhu, Color center formation in  $\alpha$ -Al<sub>2</sub>O<sub>3</sub> induced by high energy heavy ions, *Nucl. Instr. and Meth. B* 254 (2007) 268-272.
- [55] A. Berthelot, S. Hémon, F. Gourbilleau, C. Dufour, B. Domengès, E. Paumier, Behaviour of a nanometric SnO<sub>2</sub> powder under swift heavy-ion irradiation: From sputtering to splitting, *Phil. Mag. A* 80 (2000) 2257-2281.
- [56] S. Hémon, C. Dufour, A. Berthelot, F. Gourbilleau, E. Paumier, S. Bégin-Collin, Structural transformation in two yttrium oxide powders irradiated with swift molybdenum ions, *Nucl. Instr. and Meth. B* 166 (2000) 339-344.
- [57] H.J. Matzke, P.G. Lucuta, T. Wiss, Swift heavy ion and fission damage effects in UO<sub>2</sub>, *Nucl. Instrum. Methods B* 167 (2000) 920-926.
- [58] S. Moll, L. Thomé, L. Vincent, F. Garrido, G. Sattonnay, T. Thomé, J. Jagielski, J. M. Costantini, Damage induced by electronic excitation in ion-irradiated yttria-stabilized zirconia, *J. Appl. Phys.* 105 (2009) 023512-12p.
- [59] F. X. Zhang, M. Lang, J. M. Zhang, Z. Q. Cheng, Z. X. Liu, J. Lian, R. C. Ewing, Phase transition and abnormal compressibility of lanthanide silicate with the apatite structure, *Phys. Rev. B* 85 (2012) 214116-6p.
- [60] Y. Zhang, D.S. Aidhy, T. Varga, S. Moll, P.D. Edmondson, F. Namavar, K. Jin, C.N. Ostrouchov, W.J. Weber, The effect of electronic energy loss on irradiation-induced grain growth in nanocrystalline oxides, *Phys. Chem. Chem. Phys.* 16 (2014) 8051-8059.
- [61] C.L. Tracy, M. Lang, J. M. Pray, F. Zhang, D. Popov, C. Park, C. Trautmann, M. Bender, D. Severin, V.A. Skuratov, R.C. Ewing, Redox response of actinide materials to highly ionizing radiation, *Nature Com.* 6 (2015) 6133-9p.
- [62] S. Klaumünzer, M. Bender, A. Romanenko, D. Severin, Ion-Beam induced grain rotation in nanocrystalline alumina, *GSI Report 2015-1* (2015) 260, APPA-MML-MR-08.
- [63] R. Hanada, Effect of the interstitial cluster on the lattice expansion of irradiated metals, *Transactions of the Japan Institute of Metals* 12 (1971) 192-196.
- [64] Z. Zhu, P. Jung, Dimensional changes of Al<sub>2</sub>O<sub>3</sub> and SiC, proton irradiated under tensile stress, *J. Nucl. Mater.* 212 (1994) 1081-1086.
- [65] S.J. Zinkle, V.A. Skuratov, D.T. Hoelzer, On the conflicting roles of ionizing radiation in ceramics, *Nucl. Instr. and Meth. B* 191 (2002) 758-766.

## TABLES

Layer ( $\mu\text{m}$ )	0 - 4.5	4.5 - 9.4
Layer thickness , t, ( $\mu\text{m}$ )	4.5	4.9
Percentage of depth (t/9.4)	48%	52%
Incidence angle $1^\circ$	100%	0%
Incidence angle $2^\circ$	65 - 70 %	30 - 35 %

**Table I:** Fraction of the X-Ray diffracted signal coming from the layers located at 0 - 4.5  $\mu\text{m}$  and 4.5 - 9.4  $\mu\text{m}$ .

## FIGURES

**Figure 1:** (Colour online) Electronic stopping power  $S_e$  (left – open blue square), nuclear stopping power  $S_n$  (left - full blue circle) and number of displacement per atom (right – full red triangle, calculated for a fluence of  $1 \cdot 10^{14}$  Xe.cm<sup>-2</sup>) for Al<sub>2</sub>O<sub>3</sub> irradiated by 92 MeV Xe as a function of the depth, calculated with the experimental density (bottom axis) and theoretical density (top axis). The hashed region shows the depth probed by X-ray diffraction at a grazing incidence of 2° (9.4 μm, called thick slice) and 1° (4.5 μm, called thin slice).

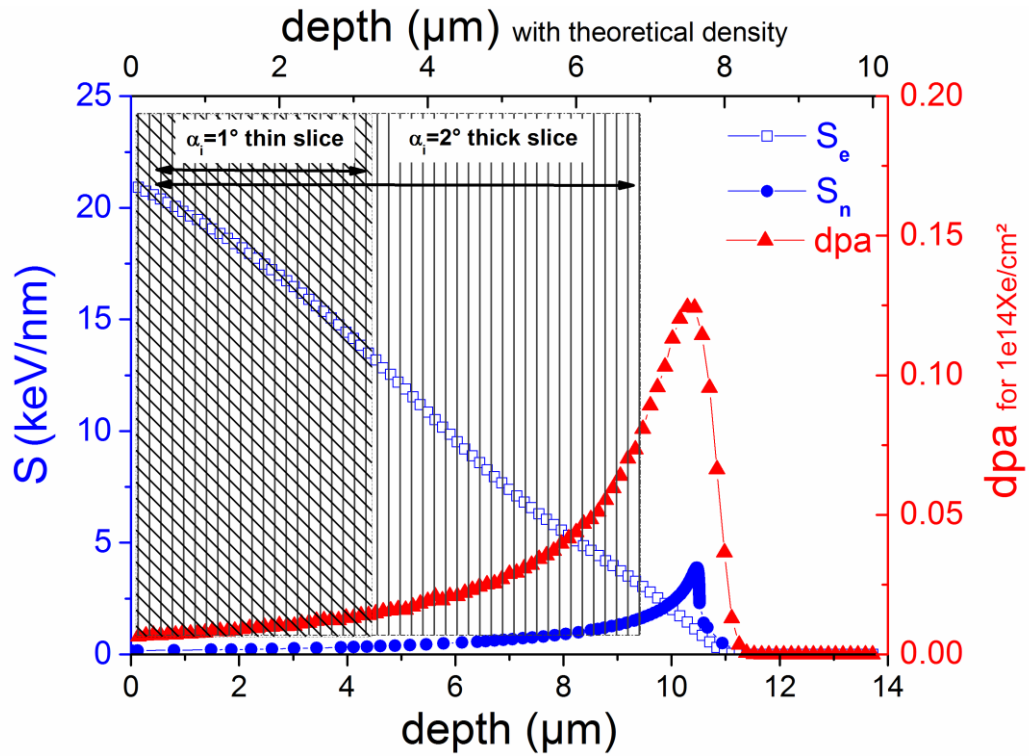
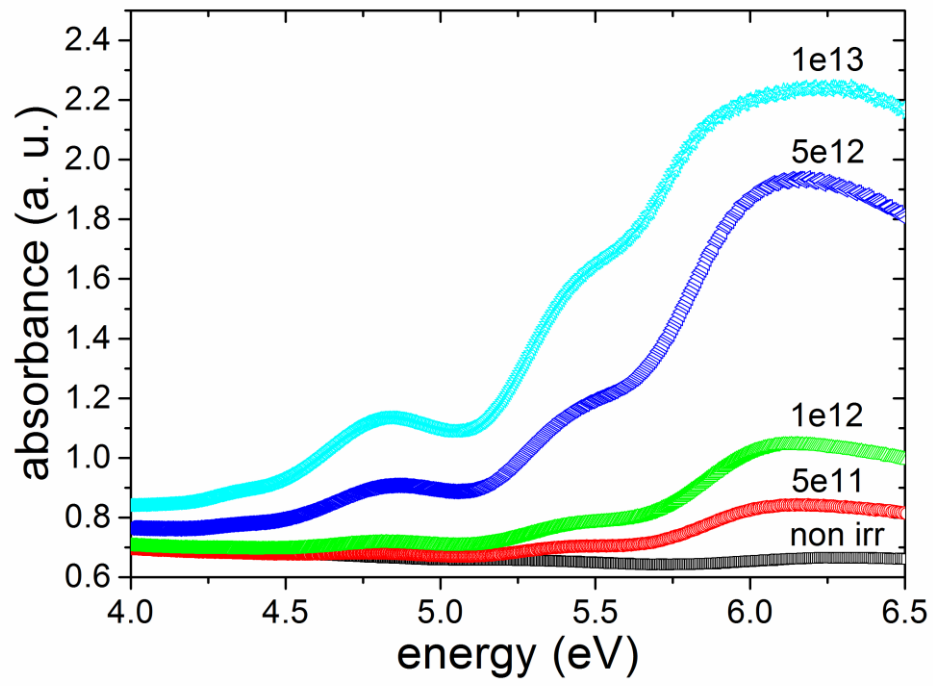
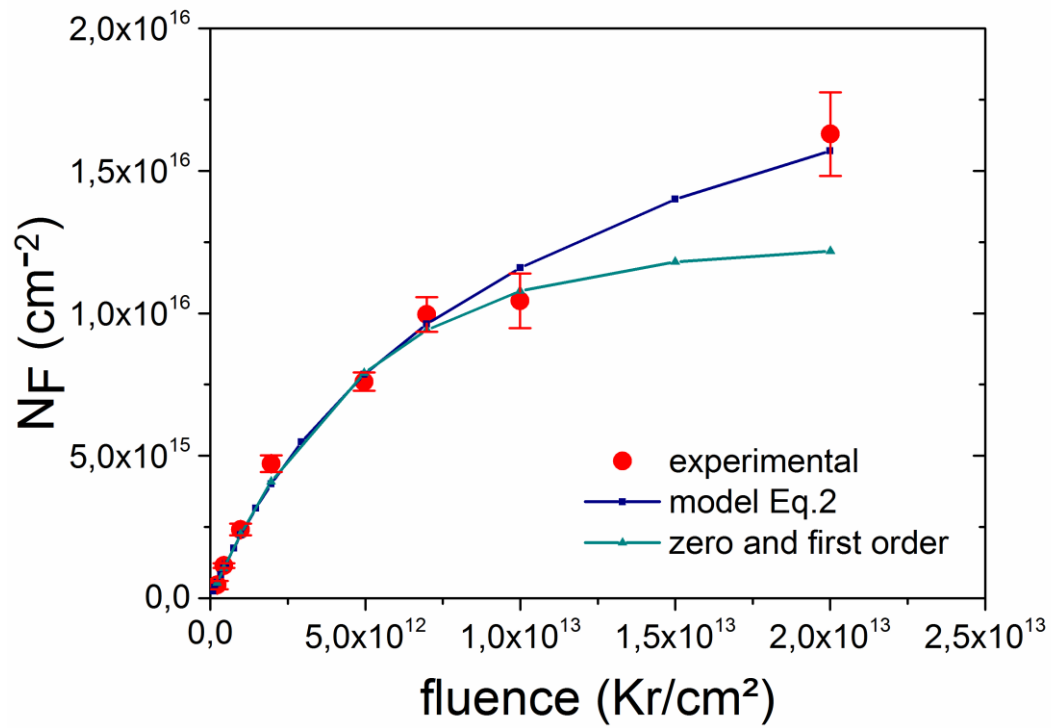


Figure 2: (Colour online) Optical absorption spectra of irradiated sapphire with 74 MeV Kr ions.



**Figure 3:** (Colour online) Area density of F centre defects ( $N_F$ ) versus Kr ion fluence, experimental values calculated with Smakula's formula and simulations by the model of F centre concentration described in the text (Eq. 2) and the classical fit using zero order creation and first order destruction kinetics for point defect creation.



**Figure 4:** (Colour online) X-ray diffraction patterns as function of Xe fluence for two grazing incidence of  $2^\circ$  and  $1^\circ$  for  $\text{Al}_2\text{O}_3$  pellet. The reflection indexation is marked on the non-irradiated patterns. The Rietveld refinements are added with experimental data (open circle), calculated data (blue line on top) and difference between experimental and calculated data (black line on bottom). Fluences [ $\text{cm}^{-2}$ ] are quoted in the figure.

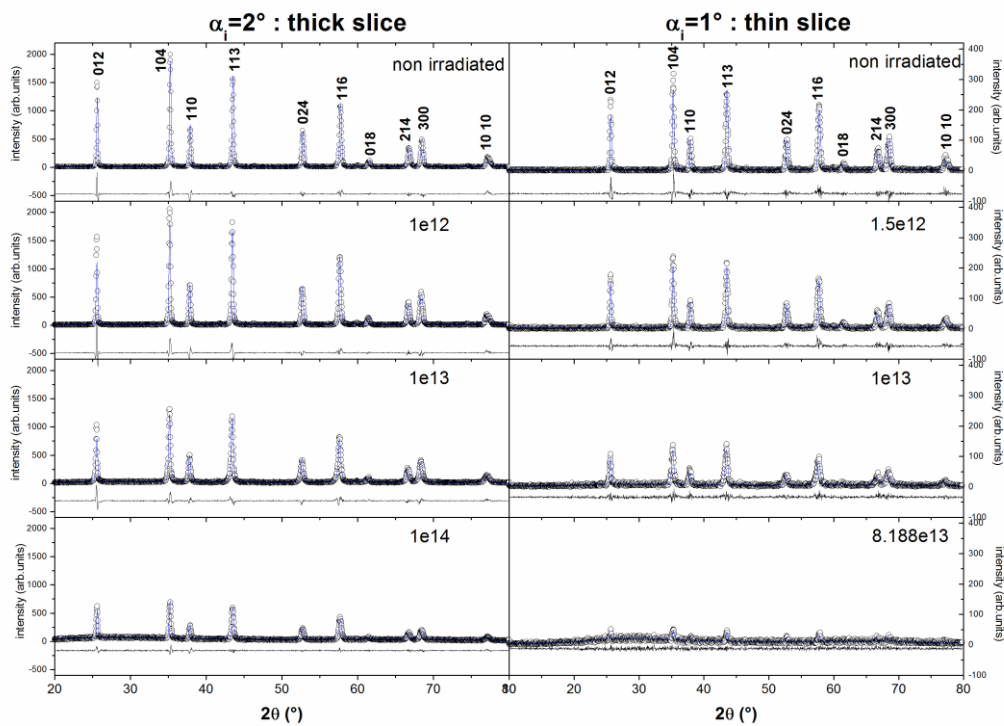


**Figure 5:** (Colour online) Amorphous fraction versus ion fluence for  $\text{Al}_2\text{O}_3$  pellet measured in GI-XRD at (a)  $2^\circ$  for Xe irradiation, (b)  $1^\circ$  for Xe irradiation and (c)  $1^\circ$  for Kr irradiation. Fractions are extracted from net area ratio (grey full symbol), from scale factor ratio (black full circle) and the fits correspond to single impact model (red), double impact model (blue) and triple impact model (green).

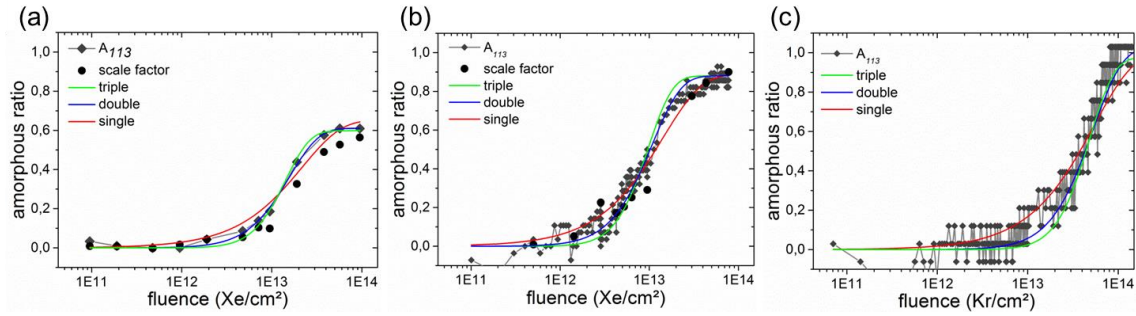


**Figure 6:** XTEM observations on a)  $\text{Al}_2\text{O}_3$  pellet irradiated by 92 MeV Xe with  $8 \cdot 10^{13}$  ions/cm<sup>2</sup>, b) a zoom of the free-defect region beyond 7  $\mu\text{m}$ , c) a zoom of the region 4 - 7  $\mu\text{m}$  showing the defect presence inside the core of the grain and an amorphous shell, d) a diffraction pattern of the region 0 - 4  $\mu\text{m}$  showing the amorphous state, and e) (0001)- $\text{Al}_2\text{O}_3$  single crystal irradiated by 92 MeV Xe with  $2 \cdot 10^{14}$  ions/cm<sup>2</sup> and the diffraction patterns corresponding to the two zones: amorphous at the surface and crystalline in depth.

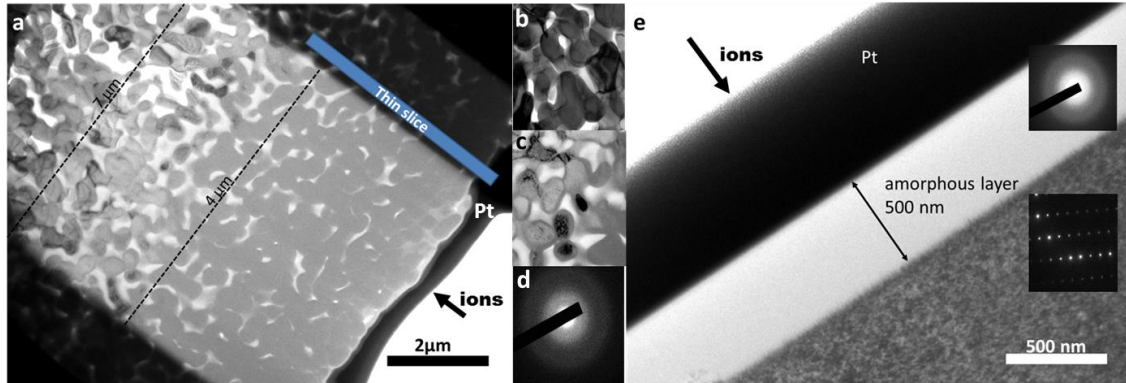
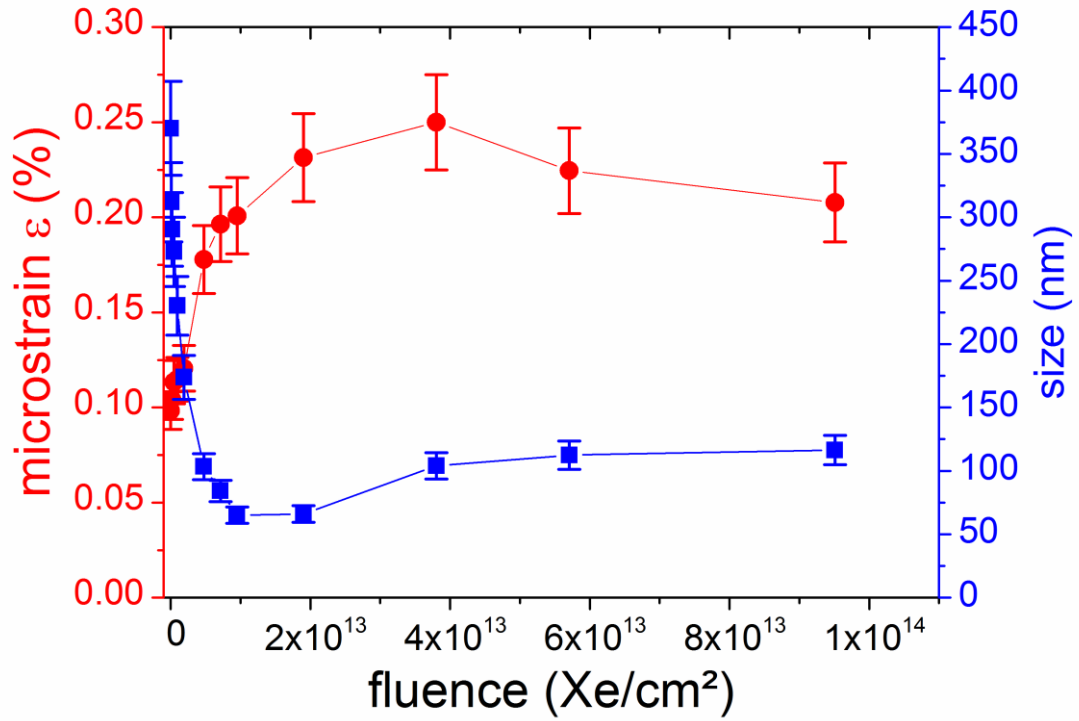
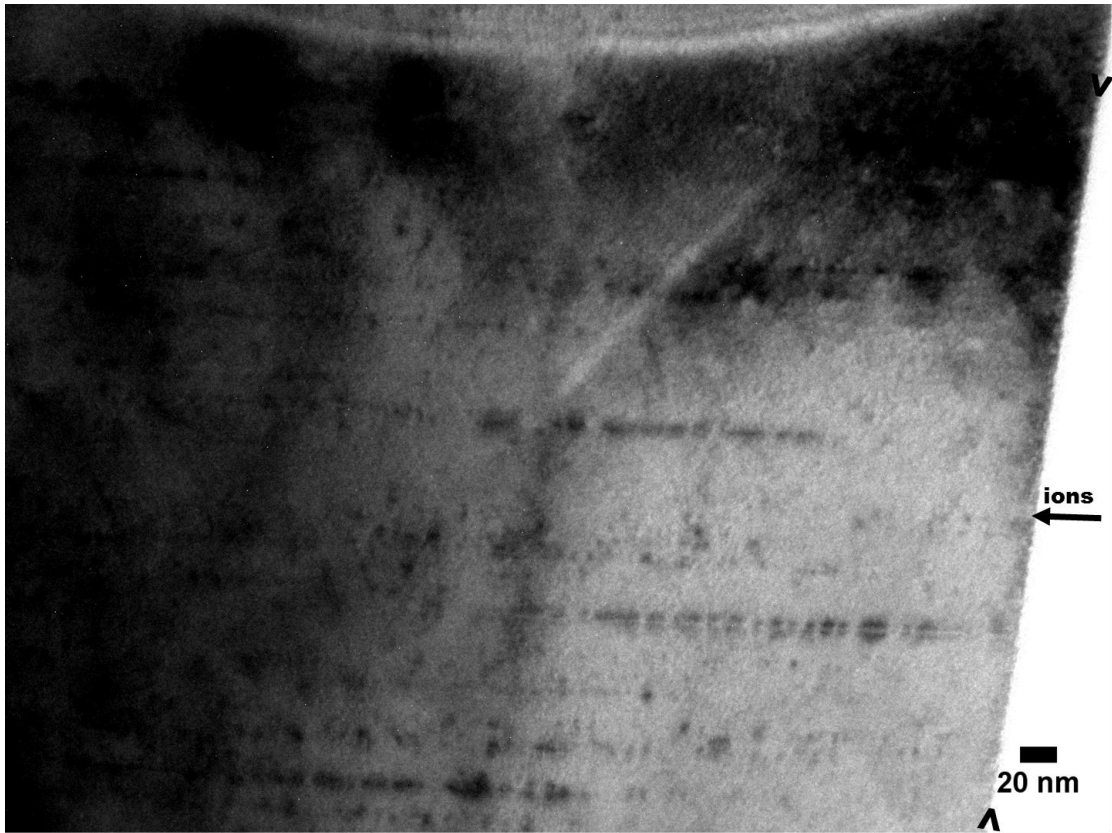


Figure 7: (Colour online) Microstructural evolution, coherent domain size (right - blue full square) and microstrain (left - red full circle) as a function of Xe fluence in thick slice of  $\text{Al}_2\text{O}_3$  pellet.



**Figure 8:** XTEM image of  $\text{Al}_2\text{O}_3$  single crystal after Xe irradiation at fluence of  $2 \cdot 10^{11}$  ions/cm<sup>2</sup>, the sample surface is highlighted by two black arrows.



**Figure 9:** XTEM observations on Al<sub>2</sub>O<sub>3</sub> pellet irradiated by 92 MeV Xe with 8·10<sup>13</sup> ions/cm<sup>2</sup>, a) a zoom of the intermediate area (4 - 7 μm), b) the intermediate area and the diffraction pattern of one grain showing the slight disorientation of domains and c) HRTEM and FFT showing the crystalline core and amorphous shell structure of the grains in the intermediate area.

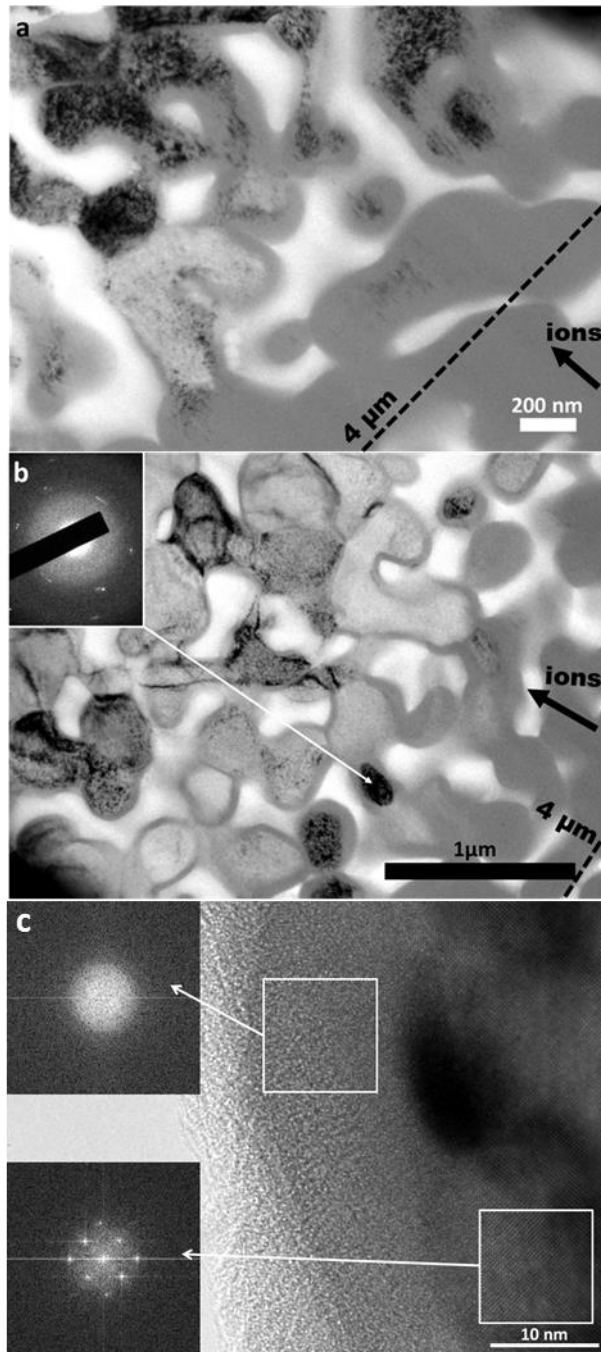


**Figure 10:** (Colour online) Variation of the atomic coordinates as function of Xe fluence in thick slice of  $\text{Al}_2\text{O}_3$  pellet. The aluminium Wyckoff position (green full triangle) in space group  $R\bar{3}c$  is (12c with  $z_0 = 0.352$ ) and the oxygen Wyckoff position (red full circle) is (18e with  $x_0 = 0.312$ ).

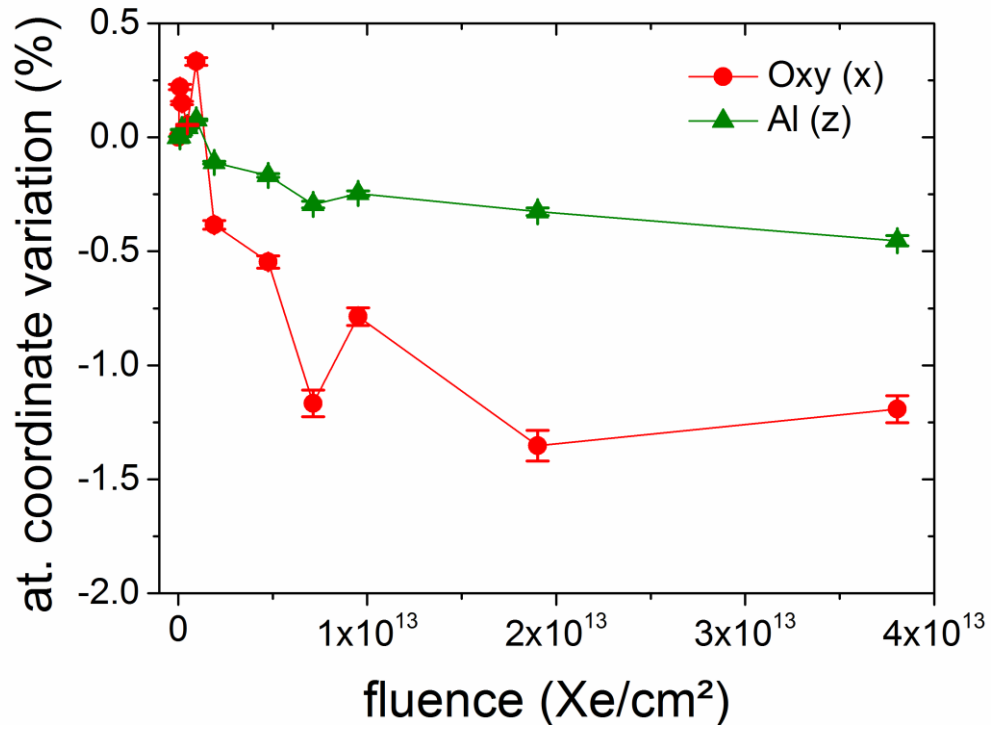


**Figure 11:** (Colour online) Variation of the unit-cell volume as function of Xe fluence in thin (green full triangle) and thick (blue full circle) slices of  $\text{Al}_2\text{O}_3$  pellet.

